

Thermal durability and interface stability of layered Yb-Gd-Y-based thermal
barrier coatings in thermal cyclic exposure

Sung-Hoon Jung¹, Zhe Lu¹, Yeon-Gil Jung^{1,*}, Dowon Song², Ungyu Paik², Baig-Gyu Choi³,
In-Soo Kim³, Xingye Guo⁴, and Jing Zhang⁴

¹School of Materials Science and Engineering, Changwon National University,
Changwon, Gyeongman 641-773, Republic of Korea

²Department of Energy Engineering, Hanyang University, Seoul 133-791
Republic of Korea

³High Temperature Materials Research Group, Korea Institute of Materials Science, 797
Changwondaero, Changwon, Gyeongnam 641-831, Republic of Korea

⁴Department of Mechanical Engineering, Indian University-Purdue University Indianapolis,
Indianapolis, IN 46202, USA

*Corresponding author. Tel: +82-55-213-3712

E-mail: jungyg@changwon.ac.kr

This is the author's manuscript of the article published in final edited form as:

Jung, S. H., Lu, Z., Jung, Y. G., Song, D., Paik, U., Choi, B. G., ... & Zhang, J. (2016). Thermal durability and fracture behavior of layered Yb-Gd-Y-based thermal barrier coatings in thermal cyclic exposure. *Surface and Coatings Technology*. <http://dx.doi.org/10.1016/j.surfcoat.2016.09.032>

Abstract

The effects of structural design on the thermal durability of Yb-Gd-Y-based thermal barrier coatings (TBCs) were investigated through thermal cyclic exposure tests, such as furnace cyclic thermal fatigue (FCTF) and jet engine thermal shock (JETS) tests. The effects of composition in the bond coat and feedstock purity for the buffer layer on its lifetime performance were also examined. To overcome the drawbacks of Yb-Gd-Y material with poor thermal durability due to poor mechanical properties and low coefficient of thermal expansion, a buffer layer was introduced in the Yb-Gd-Y-based TBC systems. In the FCTF tests, the TBC with the Co–Ni-based bond coat and the buffer layer of regular purity showed a longer lifetime performance than other TBCs, especially the TBCs without the buffer layer. In the JETS tests, the TBC with the Ni-based bond coat and the buffer layer of high purity showed a sound condition after 2000 cycles, showing better interfacial stability for TBC with the Ni-based bond coat rather than that with the Co–Ni-based bond coat in the single layer coatings without the buffer layer. The buffer layer effectively enhanced the thermal durability in slow temperature change, while the bond-coat composition and the feedstock purity for the buffer layer were found to be important factor to improve the thermal durability of the TBC in fast temperature change. Finally, these research findings allow us to control the structure, composition, and feedstock purity in TBC system for improving the thermal durability in cyclic thermal environments.

Keywords: Thermal barrier coating; Buffer layer; Composition; Purity; Thermal durability.

1. Introduction

Thermal barrier coatings (TBCs) have been widely used to protect the hot-section components of turbines and combustors for aircraft and land-based gas turbines from hot gases [1,2]. The TBCs accommodate the increase in operating temperature in turbine engines, reducing the substrate temperature of hot-section components. To improve fuel efficiency with increasing turbine inlet temperature (TIT), many researchers have attempted to design a cooling system for the turbine and combustor components, and develop substrate and TBC materials [3–6]. TBCs were first introduced to the gas turbine industry in the mid-1970s, after which the most widely used ceramic top-coat material has been 7–8 wt% yttria-doped stabilized zirconia (7-8YSZ) because it provides the best performance in high-temperature applications [7]. However, a commercial TBC material, 7–8YSZ, has been limited with poor phase stability and low sintering resistance as the TIT has increased in gas turbine engines [8, 9]. Therefore, alternative TBC materials are required with better phase stability, higher chemical inertness, lower thermal conductivity, and higher sintering resistance.

The most effective approach to meeting these needs appears to be the use of low thermal conductivity materials of RE-stabilized cubic zirconia (where RE indicates a rare-earth element) type for the outer ceramic layer [10–12]. The advanced TBCs with a low thermal conductivity have been continuously investigated with zirconate materials doped with lanthanum, gadolinium (Gd), ytterbium (Yb), etc. [13–15]. One of the promising leading candidates for advanced TBC materials is the Yb-Gd-Y-stabilized zirconia (hereinafter YGYZ). The YGYZ coating has better oxidation resistance, improved sintering resistance, higher calcium–magnesium–aluminum–silicate (CMAS) resistance, excellent phase stability, and lower thermal conductivity than YSZ coating; it has thermal conductivity of 0.80–1.24 $\text{W}\cdot(\text{m}\cdot\text{K})^{-1}$ for bulk YGYZ and of 2.1 $\text{W}\cdot(\text{m}\cdot\text{K})^{-1}$ for bulk 8YSZ [16–19]. The principal drawback of YGYZ coating is its low coefficient of thermal expansion (CTE), which does

not match the bond coat with a relatively large CTE; CTE is $9\text{--}10\times 10^{-6}\cdot\text{K}^{-1}$ for bulk YGYZ, $10.5\text{--}11.5\times 10^{-6}\cdot\text{K}^{-1}$ for bulk 8YSZ, and $15.0\times 10^{-6}\cdot\text{K}^{-1}$ at 1000 °C for Ni-based bond coat [20–22]. Therefore, the YGYZ coating can be easily delaminated because of the CTE mismatch between the YGYZ top coat and intermetallic bond coat. Another reason for the relatively short thermal durability of YGYZ coating is its low fracture toughness (K_{IC}) (K_{IC} is 0.95–1.25 $\text{MPa}\cdot\text{m}^{1/2}$ for YGYZ coating, and 1.85–2.23 $\text{MPa}\cdot\text{m}^{1/2}$ for 8YSZ coating) [23]. K_{IC} describes the ability of fracture resistance to maintain cracks in the material without the propagation of cracks. Therefore, K_{IC} should be improved to enhance the thermal durability of the YGYZ coating. In addition, YGYZ coating is less compatible with thermally grown oxide (TGO) layer than 8YSZ coating, resulting in premature failure of YGYZ-based TBC in working environments [24, 25].

One of the solutions to improve the thermal durability of YGYZ coatings as mentioned above is the layered TBC with multifunctions through structural design [26]. Many studies reported that a double-layer TBC exhibits a higher level of durability and reliability relative to a single YSZ coating [27, 28]. The buffer layer as a stress accommodating layer during thermal cycling can also be designed with a double-layer coating (DLC) to reduce stress levels and ensure thermal durability [29, 30]. Therefore, the YGYZ-based layered TBC system is believed to provide a good heat-insulating performance because the top coat is made of YGYZ material with intrinsic low thermal conductivity, and the layered structure improves the thermal durability, as the buffer layer between the top and bond coats reduces the CTE mismatch. However, the failure or delamination mechanisms in the YGYZ-based layered TBCs are not fully understood.

The high-velocity oxy-fuel (HVOF) process is a very useful for forming bond coats with a dense microstructure and a high adhesive strength in TBCs and its development has been gaining attention for TBC applications [31–33]. There is a wide range of metallic alloys

owing to its outstanding resistance to oxidation and corrosion [34], normally consisting of a MCrAlY bond coat, where M = nickel (Ni), cobalt (Co), or a combination of them (Co/Ni). The characteristics of Ni are high corrosion resistance and high melting point; Co can give temperature stability, corrosion, and wear resistance; Cr can improve hot corrosion resistance; Al can improve ductility, determining oxidation degree related with TGO; and Y can improve adherence to the oxide layer. The Co–Ni-based bond coat is widely used because of their superior thermomechanical properties [35, 36]. Usually, the bond coat of TBC system at high temperature involves Co because of the high-temperature oxidation resistance, thus enhancing the cycle life of TBCs [36]. Even though the working temperature of gas turbines increases continuously and reaches to 1600 °C, the surface temperature of components (the surface of top coat), such as blade and vane, is still within 1100 °C in real environments, owing to the improvement of cooling system. Therefore, the thermal durability of TBCs with and without Co additive bond coats should be analyzed in the working condition, which has not been studied yet.

Therefore, in this study, to understand the failure mechanism in the YGYZ-based TBC, the effects of structural design and bond coat species on the thermal durability and fracture behavior of the single-layer coating (SLC) and DLC TBC systems were investigated through thermal cyclic exposure, namely the furnace cyclic thermal fatigue (FCTF) test with slow and small temperature change and the jet engine thermal shock (JETS) test with fast and large temperature change. The relationship between thermal durability and coating structure in the YGYZ-based TBC systems is discussed, with a focus on the microstructure evolution and mechanical properties before and after cyclic thermal exposure.

2. Experiment procedure

2.1 Preparation of TBC samples

A nickel-based directionally solidified superalloy (nominal composition of 65.0Ni–10.0Cr–7.5Ta–7.0W–5.0Al–4.4Co–1.0Ti–0.08C–0.01Zr–0.01B) was used as a substrate. The dimensions of the coin-shaped sample were 25 mm and 5 mm in diameter and thickness, respectively. The substrate was sand-blasted using alumina powder with particle size of 60 mesh, and then the high velocity oxygen fuel spraying (HVOF) process using a Diamond Jet–2600 DJM (Sulzer Metco Holding AG, Switzerland) was conducted for a bond coat within 2 h. Two kinds of feedstock powder with different compositions were used to prepare the bond coat (AMDRY 9951, Sulzer Metco Holding AG, nominal composition of Co–32Ni–21Cr–8Al–0.5Y in wt% and particle size of 5–37 μm , and AMDRY 9624, Sulzer Metco Holding AG, nominal composition of Ni–22Cr–10Al–1.0Y in wt% and particle size of approximately 38 μm). Two YSZ buffer layers were deposited on the bond coat using two feedstock powders (METCO 204 C-NS with regular purity: 8.0Y₂O₃–0.7SiO₂–0.2TiO₂–0.2Al₂O₃–0.2Fe₂O₃ doped in ZrO₂ and METCO 204 C-XCL with high purity: 8.0Y₂O₃–0.05SiO₂–0.05TiO₂–0.05Al₂O₃–0.05Fe₂O₃ doped in ZrO₂, Sulzer Metco Holding AG, Switzerland, particle size of 45–140 μm , D50 of 68–77 μm). The YGYZ top coat was coated on each bond coat or each buffer layer using a commercial feedstock powder (METCO 206A, Sulzer Metco Holding AG, Switzerland, 9.5Y₂O₃–5.6Yb₂O₃–5.2Gd₂O₃ doped in ZrO₂, particle size of 45–125 μm , D50 of 50–70 μm). The buffer and top-coat layers were sprayed following the air plasma spraying (APS) method using the 9MB coating system (Sulzer Metco Holding AG, Switzerland). A schematic diagram of the structural design employed in this study is shown in Fig. 1. The thicknesses of the bond and top coats were designed as $250 \pm 50 \mu\text{m}$ and $600 \pm 50 \mu\text{m}$, respectively, in the SLC TBCs. The thicknesses of the buffer layer and the top coat are designed as $100 \pm 30 \mu\text{m}$ and $600 \pm 50 \mu\text{m}$, respectively, with the same bond coat thickness in the DLC TBCs. The fabrication parameters of the bond and top coats are shown in Table 1, including the buffer layer.

2.2 Thermal cyclic exposure tests

Thermal cyclic exposure tests were conducted to evaluate the thermal durability of TBC samples through two kinds of test methods, FCTF and JETS tests. The FCTF tests were performed for 1429 cycles in a specially designed furnace; one side of the sample was exposed and the other side air-cooled. The surface temperature of the sample was about 1100 °C with a temperature difference of 150 °C between the top and bottom surfaces of the sample and a dwell time of 60 min, followed by natural air cooling for 10 min at room temperature. The failure criterion was defined as 25% buckling or spallation of the top coat in the FCTF. The JETS tests using liquefied petroleum gas and oxygen were performed for 2000 cycles at a surface temperature of 1400 °C with a dwell time of 20 s, and then the sample was cooled using nitrogen gas to about 550 °C for 20 s and the surface temperature reached 150 °C before the next heating. During the tests, the surface and backside temperatures were measured using pyrometers (infrared thermometer with the wavelength of 3.9 μm, CTlaser MT, Optris, Germany). The failure criteria in JETS tests were typically more than 50% spallation of the top coat or cracked at the interface between the top and bond coats. At least three samples were tested for each condition. For clear understanding of test methods, photos of each apparatus for the FCTF and JETS tests are shown in Fig. 2. In the Fig. 2 (B), the rapid heating and cooling regions marked with red and blue circles, respectively.

2.3 Characterizations

The selected samples before and after thermal cyclic exposure tests were preprocessed to observe the cross-sectional microstructure. The samples were cut and cold-mounted using a liquid epoxy resin, and then polished using silicon carbide paper, and 3 and 1 μm diamond pastes, respectively. The cross-sectional microstructure of the TBC samples

was observed using a scanning electron microscope (SEM; Model JSM-5610, JEOL, Japan). Elemental analysis at the interface between the buffer layer and the bond coat was conducted using energy-dispersive X-ray analysis (EDS; S2700, Hitachi, Japan). Before measuring the mechanical properties, cutting, cold-mounting, and polishing processes were performed. The 2-D porosity of the top coats was measured using Image-pro Plus software (Media cybernetics, USA). The mechanical properties were characterized by two types of indentation method, nano-indentation and micro-indentation in the in-plane direction. Localized elastic modulus (E), and hardness (H) were evaluated using a nano-indenter (Nano Instruments, MTS Systems Corp., Eden Prairie, USA) with a Berkovich tip (radius of tip < 100 nm). The data were selected after indentation of up to 2,000 nm depth. The data were selected after indentation up to 50 gf (0.49 N). The relatively global H values of the bond and top coats were determined using a micro-indenter (HM-114, Mitutoyo Corp., Japan) with a Vickers tip for a load of 3 N and holding for 15 s, based on ASTM C1327-03 [37]. Ten indentations were performed to determine the standard deviation of each value. The size of indentation impression was measured using SEM and all indentations were performed at room temperature.

3. Results and discussions

3.1 Microstructure of as-prepared TBCs

The cross-sectional microstructures of as-prepared TBCs are shown in Fig. 3. The top and bond coats were well deposited with thicknesses of 580–760 and 200–320 μm in the top and bond coats, respectively, even though the sample B (Fig. 3(B-2)) showed a slightly thicker top coat than others. The measured porosity of the top coat was in the range 10.6 ~ 12.5 %, while the mean porosities for the buffer layers of the regular and high purities were 7.7 and 7.9 %, respectively. The surface temperature of coating is increased by melted

feedstock particle during coating process, causing a thermal stress. After coating process, a residual stress is imposed during cooling. Therefore, a thicker coating may cause the more thermal and residual stresses at the interface between the top and bond coats than a thin coating, but the thickness difference about $\sim 100 \mu\text{m}$ was tiny to affect the stresses generated on the interface so that the implication was negligible on thermal durability [38]. The microstructures in the bond coats of all of the TBCs prepared using the HVOF process showed a similar status with a dense microstructure, independent of feedstock powder. The buffer layers in both of the DLC TBCs could be observed as shown in Figs. 3(B) and 3(C), indicated as dotted blue lines. The buffer layer was coated with a thickness of 70–120 μm . The YGYZ top coat and the 8YSZ buffer layer showed intrinsic defects with the APS process, showing pores, un-melted particles, and splat boundaries. The TBC systems did not show any delamination or cracking at the interface between the top and bond coats or between the buffer layer and the top coat. The samples with the buffer layer showed a relatively irregular interface between the buffer layer and the top coat, while all of the samples showed a relatively smooth interface between the bond and top coats in the SLC TBCs or between the bond coat and the buffer layer in the DLC TBCs, compared with the interface between the buffer layer and the top coat, owing to the coating method [39, 40]. The particle velocity in the HVOF system for the bond coat can be produced up to 700 m/sec, and that in the APS system for the buffer layer is 350 m/sec. For this reason, the interface between the buffer layer and the top coat is more irregular shape than those between the bond and top coats in the SCL TBCs and between the buffer layer and the bond coat in the DLC TBCs. In addition, an indistinguishable interface without obvious large cracks was observed within the top coats, indicating that minimal thermal and residual stresses were imposed at the interfaces during coating processes.

The mechanical properties E and H of each layer, top coat and buffer layer, from nanoindentation are shown in Fig. 4. Even though the values correspond to localized properties, both the E and H values of the buffer layer were not significantly different, being 123.0 ± 23.8 and 7.2 ± 2.7 GPa (mean \pm standard deviation) for the buffer layer of regular purity, 121.0 ± 21.7 and 7.4 ± 2.7 GPa for the buffer layer of high purity buffer layer, and 113.9 ± 23.8 and 6.7 ± 3.0 GPa for the YGYZ top coat. The H values from Vickers indentation inserted in Fig. 4 showed a lower trend than those *measured by* nanoindentation, being 4.4 ± 0.3 GPa for the buffer layer and 4.1 ± 0.2 GPa for the YGYZ coating. The values obtained from localized regions by nanoindentation are higher than those from *relatively global regions*, because of its microstructural distinctions. Fewer defects such as pore, splat boundaries, and microcracks are included upon decreasing the indentation range. Usually, fracture or failure in a TBC system originates at the near-interface region, and the requirement of high mechanical properties is desired within this region [41]. However, the general mechanical properties are not much dependent on the starting feedstock powder in the as-prepared status, contrary to expectations, even though the mechanical properties of the 8YSZ buffer layer are slightly higher than those of the YGYZ top coat, due to the relatively dense microstructure.

3.2 Furnace cyclic thermal fatigue test

The FCTF tests were performed for all samples, and the numbers of cycle-to-failure and its status are summarized in Table 2. The cross-sectional microstructures of each TBC with different bond coats are shown in Fig. 5 after the FCFT tests. For the SLC TBCs, the top coats were completely delaminated between 170–238 and 323–340 cycles for the Co–Ni-based and Ni-based bond coats, respectively. The lifetime of all samples with all layered structure was longer than that without the buffer layer. The relatively early failure of the SLC TBCs can be

attributed to its lower fracture toughness of the YGYZ top coat, compared with the buffer layer. The DLC TBCs with the Co–Ni-based bond coat were sustained for a longer lifetime than those with the Ni-based bond coat, independent of the buffer layer species. In the FCTF tests, although the SLC TBC with the Ni-base bond coat showed longer lifetime performance than that with the Co–Ni-based bond coat, the longest lifetime performance was shown in the DLC TBC with the Co–Ni-based bond coat and the buffer layer of regular purity due to the temperature stability of composition and the relatively thick thickness, respectively [4, 35, 36]. The fracture originated at the interface between the top coat and the buffer layer or within the top coat near the interface, independent of the buffer layer species and the bond-coat composition. Usually fracture or delamination in TBC system happens within 100 μm from the interface of the top and bond coats [41, 42]. Therefore, the mechanical properties at the near-interface should be enhanced to improve fracture resistance through crack propagation.

In high-magnification cross-sectional microstructures at the interface between the bond and top coats, and between the bond coat and the buffer layer, the top-coat layer was fully delaminated after the FCTF test while the YGYZ layer was left with the thickness about 60–70 μm as shown in Fig. 6. Especially both of the DLC TBCs contain the buffer and YGYZ layers after the FCTF test and the remained YGYZ layer in the TBC with the buffer layer of high purity is thicker than that of regular purity, indicating that a catastrophic failure of TBC resulted from the full delamination during actual operation can be prevented by introducing the buffer layer of high purity. On the other hand, it was found that the TGO growth behavior was affected by the bond coat composition. The TGO layer in the TBCs with the Co–Ni-based bond coat formed well with a thickness of $6.3 \pm 2.5 \mu\text{m}$. The thickness of the TGO layer is strongly dependent on the exposure time and bond-coat composition, consisting of two regions: the gray color (position (1) in Fig. 6(B-1)) formed later and the black color

(position (2) in Fig. 6(B-1)) formed earlier. The elemental compositions of TGO layers are given in Table II. It can be seen that the gray region (position (2)) is composed of Ni, Co, Cr, O and Al elements, whereas the black region (position (1)) is mainly composed of Al and O elements. Even though Ni, Co, and Cr elements were detected together in position (1) of Fig. 6(B-1), it can be a negligible amount and from near the detected spot. While the TBCs with the Ni-based bond coat formed a thinner TGO thickness of $3.7 \pm 1.2 \mu\text{m}$, it showed a more serious internal oxidation on the bond coats near the interface compared with those *with the Co-Ni-based bond coat which has superior oxidation resistance. [43]*. For the Ni-based bond coat (Fig. 6(B-2)), the gray region (position (2)) is composed of Ni, Cr, O, and Al elements, whereas the black region (position (1)) is mainly composed of Al and O elements. The EDS analysis indicated that Co element in the bond-coat composition can easily form the TGO layer, and the TBCs with the Co-Ni-based bond coat showed an element diffusion area (element-depletion area), near the interface between the top coat or the buffer layer and the bond coat. Although YGYZ top coat was directly deposited on the bond coat, there was no additional element in TGO layer resulted from chemical reaction between the YGYZ and the bond coats. Gue et. al. performed hot corrosion resistance test for the $\text{Gd}_2\text{Zr}_2\text{O}_7$ - and YSZ-based coatings, and they concluded the $\text{Gd}_2\text{Zr}_2\text{O}_7$ -based coating is more thermally and chemically stable than the YSZ-based coating [44].

The bond coat is inevitably oxidized and the TGO layer is formed at the interface between the bond and top coats with a thickness of 3.7–6.3 μm . The thickness of the TGO layer gives a difference in stress intensity factors. The thicker TGO layer results in a markedly large stress intensity factor during the intermediate and late stage of crack growth, although it is slightly lower during the initiation of crack. As a result, the fast growth rate of the TGO layer leads to the short lifetime performance of the TBC [45]. The TBC is a multilayer coating system including superalloy, intermetallic bond coat, TGO layer, and

ceramic top coat. Therefore, the volume change accompanied by the thermal cycling process is different due to the different CTEs. The bond coat has a similar CTE as the substrate, so lower thermal and residual stresses are created at the interface between the bond coat and the substrate during the heating and cooling processes, respectively. The main fracture or failure source considered between the bond and top coats is the residual stress due to the mismatch of CTEs among the corresponding parameters of E , Poisson's ratio, and CTE, which is introduced during cooling. In addition, in the layered structure, the thermal and residual stresses generated among layers due to the CTE mismatch become the most important reasons for failure [3]. The CTE value of Ni-based bond coat is usually $\sim 15 \times 10^{-6} \cdot \text{K}^{-1}$ at 1000 C, which is much larger than those of ceramic top coats: $9\text{--}10 \times 10^{-6} \cdot \text{K}^{-1}$ for bulk YGYZ and $10.5\text{--}11.5 \times 10^{-6} \cdot \text{K}^{-1}$ for bulk 8YSZ [26–28]. Therefore, large CTE is preferred for the ceramic top coat to enhance the thermal durability.

3.3 Jet engine thermal shock test

The numbers of cycle-to-failure and its status in JETS tests are summarized in Table 1. The surface micrographs of TBCs after JETS tests are shown in Fig. 7. As shown in Fig.7 (C-2), the *DLC* TBC with the buffer layer of high purity and the Ni-based bond coat did not show any fracture evidence after JETS tests for 2000 cycles—the broken part in the edge was due to the sample holder. In Figs. 7(A-1) and 7(A-2), the delamination (or fracture) area of SLC TBCs was more than 50% within the top coat near the interface of the top and bond coats. In the DLC TBCs, damage morphology was very similar to that in the SLC TBCs. Cracking started from the center, then extended to the edge and led to coating fracture. The failure in the DLC TBCs occurred within the top coat or at the interface of the top coat and the buffer layer, showing a delamination area of more than 50%.

The cross-sectional microstructures of TBCs after JETS tests are shown in Figs. 8 and 9. For the SLC TBCs, the TBCs were delaminated within the top coat near the interface of the top and bond coats in the range of 510–1130 cycles for the Co-Ni based bond coat and in the range of 350–678 cycles for the Ni-based bond coat. Lower CTE of the top coat, the YGYZ layer, may lead to higher stress generation at the interface between the top and bond coats during JETS tests, which is a disadvantage with respect to the YSZ based TBC. The lifetime of the SLC TBC with the Co–Ni-based bond coat was far longer than that with the Ni-based bond coat. For the SLC TBC system, the thermal durability can be effectively improved by controlling the bond-coat composition. The DLC TBCs with the Co–Ni-based bond coat was delaminated at the interface between the top coat and the buffer layer or within the top coat near the interface in the range of 360–760 cycles for the buffer layer of regular purity (Fig. 8(B-1)) and 218–530 cycles for the buffer layer of high purity (Fig. 8(C-1)). The DLC TBC with the buffer layer of regular purity and the Ni-based bond coat was delaminated at the interface between the top coat and the buffer layer coat in the range of 1127–1130 cycles (Fig. 8(B-2)). The DLC TBC with the buffer layer of high purity and the Ni-based bond coat showed a sound condition without cracking or delamination, whereas a long vertical crack was found throughout the entire top coat and transverse cracks at the interface between the top coat and the buffer layer.

After the JETS test, the buffer layer of regular purity was fully delaminated at the interface between top coat and buffer layer, while a thin YGYZ layer was remained in the TBC with the buffer layer of high purity (Fig. 9(C-1)). On the other hand, any TGO scale and growth observed as shown in Fig. 9, even compared with the as-coated microstructures in Fig. 3. This is the result of the thermal barrier's characteristics of low thermal conductivity, thick coating thickness (over 600 μm), and relatively short thermal exposure time (700 min) compared with FCTF test results. When the results after the JETS test were compared with

those of the FCTF test, the growth of TGO was significantly observed with global oxidation in the bond coat in the FCTF test, while both the TGO growth and bond coat oxidation were not observed after the JETS test due to the difference of whole thermal exposure time.

In the JETS tests, once the surface of top-coat layer is exposed by direct flame, the surface temperature reaches to about 1000 °C with volume expansion, and nitrogen cooling with the vertical direction causes rapid quenching with shrinkage. Therefore, a thermal gradient from the surface to the interface can be created within the sample as the surface of the sample is exposed to the high-temperature flame—relatively high and low temperatures on the surface and at the interface, respectively. After the short heating process, partial densification occurred on the surface of the top coat. The fast cooling process causes a compressive stress on the surface of the sample, which induces intra-lamellar cracks due to the stiffness and lack of compliance. In further JETS tests, the intra-lamellar cracks formed at the initial stage will be coalesced by the in-plane tensile stress during the heating process and turned into an initial vertical crack. The initially formed vertical cracks can be propagated perpendicular to the interface due to the contraction of other parts by the in-plane compressive stress in the relatively rapid cooling process, generating visible vertical cracks with the interval of about 0.5 mm in this study, indicating that the thickness of vertical cracks is getting larger near the surface of top coat. The tensile stress out-of-plane during the cooling process due to the CTE mismatch between the top and bond coats can promote the propagation of parallel cracks created or existing at the interface or near the interface [46]. The vertical cracked TBC system can enhance the thermal durability with improved strain compliance during operations [47].

The E and H values for the TBC that survived after the JETS test are shown in Fig. 10. The H values were more sensitive to the JETS test than the E values, showing a similar E value of 113.4 ± 31.0 GPa and a slightly higher H value of 8.9 ± 3.6 GPa compared with

those of as-prepared status which E and H values are 113.9 ± 23.8 GPa and 6.7 ± 3.0 GPa. One of reasons for increasing the H value is sintering effect from direct flame exposure with the temperature above 1400 °C. However, the E and H values for the buffer layer were lower than those of as-prepared status which E and H values are 120.0 ± 21.7 GPa and 7.4 ± 2.7 GPa, being 80.0 ± 9.8 GPa and 4.8 ± 1.1 GPa, respectively. The lower values are due to the newly developed microcracks, such as intralamellar cracks and/or interlamellar cracks, during the rapid heating and cooling processes. After the JETS test, the H values from Vickers indentation showed lower values compared with those from nanoindentation, showing 3.9 ± 0.2 GPa for the buffer layer and 6.3 ± 0.2 GPa for the YGYZ coating. The higher H value of the YGYZ coating after the JETS test implies that the top coat is locally densified, and the lower H value of the buffer layer confirms the stress accumulation and the newly formed internal defects, as mentioned above.

4. Conclusions

New architectures of TBC were designed and prepared using the low thermal conductivity material, YGYZ, and the buffer layers of 8YSZ. The influences of the structural design, composition in the bond coat, and feedstock purity of the buffer layer on the thermal durability of the YGYZ-based TBC system with the top coat prepared by the APS method and the bond coat prepared by the HVOF method were investigated through the FCTF and JETS tests. The SLC and DLC TBCs showed a sound condition in the as-prepared status. The relatively early failure of the SLC TBCs in the FCTF test can be attributed to its lower fracture toughness of the YGYZ top coat, compared with the buffer layer (8YSZ). After the FCTF test, the DLC TBC with the buffer layer of regular purity and the Co–Ni-based bond coat showed a better thermal durability. However, all of the TBC samples were delaminated at the interface between the YGYZ top coat and the bond coat or within the YGYZ top coat

near the interface. The DLC TBC with the buffer layer of high purity and the Ni-based bond coat was in a sound condition after 2000 cycles in the JETS tests, whereas the other TBCs were delaminated before 1130 cycles. Structural design by introducing a buffer layer enhanced thermal durability in the slow cooling environment similar to the FCTF test. However, in the fast cooling environment similar to the JETS test, the fracture behavior would be changed from fully delamination near the interface to partial delamination or within the top coat by introducing the buffer layer of high purity and controlling the bond-coat composition.

Acknowledgments

This work was supported by a National Research Foundation of Korea (NRF) grant funded by the Korean Government (grant number 2011-0030058); the Ministry of Science, ICT and Future Planning (grant number 234-4413.C); the Power Generation & Electricity Delivery of the Korea Institute of Energy Technology Evaluation and Planning (KETEP); the Korean Government Ministry of Trade, Industry and Energy (grant numbers 2013-101010-170C/2011T100200224); and the United States Department of Energy (grant number DE-FE0008868, program manager: Richard Dunst).

References

- [1] D.R. Clarke, S. R. Phillpot, Thermal barrier coating materials, *Mater. Today* 8 (6) (2005) 22–29.
- [2] R. Vassen, M. O. Jarligo, T. Steinke, D. E. Mack, D. Stöver, Overview on advanced thermal barrier coatings, *Surf. Coat. Technol.* 205 (4) (2010) 938–942.
- [3] N.R. Padture, M. Gell, and E.H Jordan, Thermal Barrier Coatings for Gas-Turbine Engine Applications, *Prog. Mater. Sci.* 296 (5566) (2002) 280–284.
- [4] D.R. Clarke, M. Oechsner, N.P. Padture, Thermal-barrier coatings for more efficient gas turbine engines, *MRS Bulletin* 37 (10) (2012) 891–898.
- [5] D.R. Clarke, C. Levi, Materials design for the next generation thermal barrier coatings, *Annual Review of Mater. Res.* 33 (2003) 383–417.
- [6] R.A. Miller, Current status of thermal barrier coatings—An overview, *Surf. Coat. Technol.* 30 (1) (1987) 1–11.
- [7] R.A. Miller, Thermal barrier coatings for aircraft engines: history and directions, *JTST*, 6 (1997) 35-42.
- [8] S. Paul, A.Cipitria, S.A.Tsipas, T.W.Clyne, Sintering characteristics of plasma sprayed zirconia coatings containing different stabilisers, *Surf. Coat Technol.* 203 (8) (2009) 1069–1074.
- [9] X. Cao, R. Vassen, D. Stover, Ceramic materials for thermal barrier coatings, *J. Eur. Ceram. Soc.* 24 (1) (2004) 1–10.
- [10] G. Moskal, L. Swadźba, M. Hetmańczyk, B. Witala, B. Mendala, J. Mendala, P. Sosnowy, *J. Eur. Ceram. Soc.* 32 (9) (2012) 2025-2034.
- [11] L. Wang, L. Guo, Z. Li, H. Peng, Y. Ma, S.K. Gong, H.B. Guo, Protectiveness of Pt and $Gd_2Zr_2O_7$ layers on EB-PVD YSZ thermal barrier coatings against calcium-magnesium alumina-silicate (CMAS) attack, *Ceram. Int.* 41 (9) (2015) 1162-1169.
- [12] L. Wang, J.I. Eldridge, S.M. Guo, Thermal radiation properties of plasma-sprayed $Gd_2Zr_2O_7$ thermal barrier coatings, *Scripta Materialia* 69 (9) (2013) 674-677.
- [13] C.G. Levi, Emerging materials and processes for thermal barrier systems, *Curr. Opin. Solid State Mater. Sci.* 8(1) 2004 77-91.

- [14] X. Guo, Z. Lu, Y.G. Jung, L. Li, J. Knapp, J. Zhang, Thermal properties, thermal shock, and thermal cycling behavior of lanthanum zirconate-based thermal barrier coatings, *Metal. Mater. Trans. E*, 3E (2016) 64–70.
- [15] B.T. Richards, S. Sehr, F. de Franqueville, M.R. Begley, H.N.G. Wadley, Fracture mechanisms of ytterbium monosilicate environmental barrier coatings during cyclic thermal exposure, *Acta Mater.* 103 (2016) 448–460.
- [16] S. Lakiza, O. Fabrichnaya, Ch. Wang, M. Zinkevich, F. Aldinger, Phase diagram of the $\text{ZrO}_2\text{-Gd}_2\text{O}_3\text{-Al}_2\text{O}_3$ system, *J. Eur. Ceram. Soc.* 26 (3) (2006) 233–246.
- [17] Z.G. Liu, J.H. Ouyang, Yu. Zhou, Structural evolution and thermophysical properties of $(\text{Sm}_x\text{Gd}_{1-x})_2\text{Zr}_2\text{O}_7$ ($0 \leq x \leq 1.0$) ceramics, *J. Mater. Sci.* 43(10) (2008) 3596–3603.
- [18] J. Feng, B. Xiao, C.L. Wan, Z.X. Qu, Z.C. Huang, J.C. Chen, R. Zhou, W. Pan, Electronic structure, mechanical properties and thermal conductivity of $\text{Ln}_2\text{Zr}_2\text{O}_7$ ($\text{Ln} = \text{La}, \text{Pr}, \text{Nd}, \text{Sm}, \text{Eu}$ and Gd) pyrochlore, *Acta Mater.* 59 (4) (2011) 1742–1760.
- [19] L. Guo, H.B. Guo, H. Peng, S.K. Gong, Thermophysical properties of Yb_2O_3 doped $\text{Gd}_2\text{Zr}_2\text{O}_7$ and thermal cycling durability of $(\text{Gd}_{0.9}\text{Yb}_{0.1})_2\text{Zr}_2\text{O}_7/\text{YSZ}$ thermal barrier coatings, *J. Eur. Ceram. Soc.* 34 (2014) 1255–1263.
- [20] R. Vassen, X. Cao, F. Tietz, D. Basu, D. Stöver, Zirconates as new materials for thermal barrier coatings, *J. Am. Ceram. Soc.* 83(8) (2000) 2023–2028.
- [21] T.A. Taylor, Thermal barrier coating for substrates and process for producing it, US Patents No. 7910225 B2, 2011.
- [22] E. Bakan, D.E. Mack, G. Mauer, R. Vassen, Gadolinium zirconate/YSZ thermal barrier coatings: plasma spraying, microstructure, and thermal cycling behavior, *J. Am. Ceram. Soc.* 97(12) (2014) 4045–4051.
- [23] G. Dwivedi, V. Viswanathan, S. Sampath, A. Shyam, E. Lara-Curzio, Fracture toughness of plasma-sprayed thermal barrier ceramics: Influence of processing, microstructure, and thermal aging, *J. Am. Ceram. Soc.* 97 (9) (2014) 2736–2744.
- [24] C.G. Levi, J.W. Hutchinson, M.H. Vidal-Setif, C.A. Johnson, Environmental degradation of thermal-barrier coatings by molten deposits, *MRS Bull.* 37(10) (2012) 932–941.

- [25] J.M. Drexler, C.H. Chen, A.D. Gledhill, K. Shinoda, S. Sampath, N.P. Padture, Plasmasprayed gadolinium zirconate thermal barrier coatings that are resistant to damage by molten Ca–Mg–Al–silicate glass, *Surf. Coat. Technol.* 206 (19–20) (2012) 3911–3916.
- [26] K. Bobzin, N. Bagcivan, T. Brögelmann, B. Yildirim, Influence of temperature on phase stability and thermal conductivity of single- and double-ceramic-layer EB–PVD TBC top coats consisting of 7YSZ, $Gd_2Zr_2O_7$ and $La_2Zr_2O_7$, *Surf. Coat. Technol.* 237 (2013) 56–64.
- [27] K.S. Lee, D.H. Lee, T.W. Kim, Microstructure controls in gadolinium zirconate/YSZ double layers and their properties, *J. Ceram. Jpn.* 122(8) (2014) 668–673.
- [28] R. Vassen, F. Traeger, D. Stöver, New Thermal barrier coatings based on pyrochlore/YSZ double-layer systems, *Inter. J. App. Ceram. Technol.* 1(4) (2004) 351–361.
- [29] C.H. Wang et al., Optimized functionally graded $La_2Zr_2O_7/8YSZ$ thermal barrier coatings fabricated by suspension plasma spraying, *J. Alloys Comp.* 649 (2015) 1182–1190.
- [30] X.Y. Guo, Z. Lu, Y.G. Jung, L. Li, J. Knapp, J. Zhang, Thermomechanical properties of bilayer $La_2Zr_2O_7$ thermal barrier coatings, *Energy Technol.* (2016) 151–160.
- [31] E. Lugscheider, C. Herbst, L. Zhao, Parameter studies on high-velocity oxy-fuel spraying of MCrAlY coatings, *Surf. Coat. Technol.* 108 (1998) 16–23.
- [32] L. Zhao, M. Parco, E. Lugscheider, High velocity oxy-fuel thermal spraying of a NiCoCrAlY alloy, *Surf. Coat. Technol.* 179 (2004) 272–278.
- [33] S. Saeidi, K.T. Voisey, D.G. McCartney, The effect of heat treatment on the oxidation behavior of HVOF and VPS CoNiCrAlY coatings, *J. Therm. Spray Technol.* 18 (2) (2009) 209–216.
- [34] B. Beardsley, Thick thermal barrier coatings for diesel engines, *J. Therm. Spray Technol.* 6 (2) (1997) 181–186.
- [35] C.R.C. Lima, J. Nin, J.M. Guilemany, Evaluation of residual stresses of thermal barrier coatings with HVOF thermally sprayed bond coats using the modified layer removal method (MLRM), *Surf. Coat. Technol.* 200 (20) (2006) 5963–5972.
- [36] W. Lih, E. Chang, B.C. Wu, C.H. Chao, A. Peng, Effect of bond-coat pre-aluminization and pre-oxidation duplex pretreatment on the performance of $ZrO_2-8 \text{ wt.}\% Y_2O_3/Co-29Cr-6Al-1Y$ thermal-barrier coatings, *Oxid. Met.* 40 (3-4) (1993) 229–243.

- [37] ASTM C1327-03: Standard Test Method for Vickers Indentation Hardness of Advanced Ceramics.
- [38] Y. Radin, T. Kontorovich, Equivalent operating hours concept for CCPP components reliability evaluation international, Conference on Power Energy System, 13 (2012) 175–178.
- [39] F. Traeger, M. Ahrens, R. Vaßen, D. Stöver, A life time model for ceramic thermal barrier coatings, Mater. Sci. Eng. A 358 (2003) 255–265.
- [40] B. Rajasekaran, G. Mauer, R. Vaßen, Enhanced characteristics of HVOF-sprayed MCrAlY bond coats for TBC applications, J. Therm. Spray Technol. 20 (2011) 1209–1216.
- [41] V. Viswanathan, G. Dvivedi, S. Sampath, Engineered multilayer thermal barrier coatings for enhanced durability and functional performance, J. Am. Ceram. Soc. 97 (9) (2014) 2770–2778.
- [42] A.N. Khan, J. Lu, Behavior of air plasma sprayed thermal barrier coatings, subject to intense thermal cycling, Surf. Coat. Technol. 166(1) (2003) 37–43.
- [43] A. Peng, Effect of Bond-Coat Pre-Aluminization and Pre-Oxidation Duplex Pretreatment on the Performance of ZrO₂-8 wt.% Y₂O₃ Co-29Cr-6Al-1Y Thermal Barrier Coatings, Oxidation of Metals, 40(3/4) (1993)
- [44] .H. Habibi, Li Wang, S.M. Guo, Evolution of hot corrosion resistance of YSZ, Gd₂Zr₂O₇, and Gd₂Zr₂O₇ + YSZ composite thermal barrier coatings in Na₂SO₄ + V₂O₅ at 1050 °C, J. Eur. Ceram. Soc. 32 (8) (2012) 1635-1642.
- [45] R. Eriksson, S. Johansson, H. Brodin, E. Broitman, L. Östergren, X.-H. Li, Influence of substrate material on the life of atmospheric plasma sprayed thermal barrier coatings, Surf. Coat. Technol. 232 (2013) 795–803.
- [46] J.S. Yang, J.H. Yu, X.H. Zhong, H.Y. Zhao, X.M. Zhou, S.Y. Tao, Experimental and numerical investigation of residual stresses in plasma-sprayed thermal barrier coatings, J. Inorg. Mater. 28 (2013) 1381–1386.
- [47] E.A.G. Shillington, D.R. Clarke, Spalling failure of a thermal barrier coating associated with aluminum depletion in the bond-coat, Acta Mater. 47 (4) (1999) 1297–1305.

Table captions

Table 1. Fabrication parameters for each layer in TBCs

Table 2. Summary of the numbers of cycle-to-failure and its status after each thermal exposure test

Table 3. EDS analysis for TGO layers developed after FCTF tests (at.%)

Figure captions

Figure 1. Schematic diagram for structural design employed in this study.

Figure 2. Photos of each test apparatus: (A) furnace cyclic thermal fatigue (FCTF) and (B) jet engine thermal shock (JETS).

Figure 3. Cross-sectional microstructures of as-prepared TBCs: (A) SLC TBCs, (B) DLC TBCs with the buffer layer of regular purity, and (C) DLC TBCs with the buffer layer of high purity. Each number indicates TBCs with different bond coats, Co-Ni based bond coat and Ni-based bond coat, respectively.

Figure 4. Elastic modulus (E) hardness (H) values of as-prepared TBCs obtained by nano-indentation and H values obtained by Vickers indentation.

Figure 5. Cross-sectional microstructures after FCTF tests: (A) SLC TBCs, (B) DLC TBCs with the buffer layer of regular purity, and (C) DLC TBCs with the buffer layer of high purity. Each number indicates TBCs with different bond coats, Co-Ni based bond coat and Ni-based bond coat, respectively. The numbers of cycle-to-failure corresponding to each figure are shown inside each figure.

Figure 6. High magnified cross-sectional microstructures after FCTF tests: (A) SLC TBCs, (B) DLC TBCs with the buffer layer of regular purity, and (C) DLC TBCs with the buffer layer of high purity. Each number indicates TBCs with different bond coats, Co-Ni based bond coat and Ni-based bond coat, respectively.

Figure 7. Surface micrographs of TBCs after JETS tests: (A) SLC TBCs, (B) DLC TBCs with the buffer layer of regular purity, and (C) DLC TBCs with the buffer layer of high purity. Each number indicates TBCs with different bond coats, Co-Ni based bond coat and Ni-based bond coat, respectively.

Figure 8. Cross-sectional microstructures after JETS tests: (A) SLC TBCs, (B) DLC TBCs with the buffer layer of regular purity, and (C) DLC TBCs with the buffer layer of high purity. Each number indicates TBCs with different bond coats, Co-Ni based bond coat and Ni-based bond coat, respectively. The numbers of cycle-to-failure corresponding to each figure are shown inside each figure.

Figure 9. High magnified cross-sectional microstructures after JETS tests: (A) SLC TBCs, (B) DLC TBCs with the buffer layer of regular purity, and (C) DLC TBCs with the buffer layer of high purity. Each number indicates TBCs with different bond coats, Co-Ni based bond coat and Ni-based bond coat, respectively.

Figure 10. Elastic modulus (E) hardness (H) values measured by nano-indentation and H values obtained by Vickers indentation for TBCs survived after the JETS test.

Table 1. Fabrication parameters for each layer in TBCs

Table 2. Summary of the numbers of cycle-to-failure and its status after each thermal exposure test

Sample	Bond coat	Top coat	FCTF test/Status	JETS test/Status
A-1	AMDRY 9951 (Co-Ni-based)	METCO 206A	170–238 cycles/ Delamination	510–1130 cycles/ Delamination
B-1		METCO 206A /METCO C-NS	880–1096 cycles/ Delamination	360–760 cycles/ Delamination
C-1		METCO 206A /METCO C-XCL	690–696 cycles/ Delamination	218–530 cycles/ Delamination
B-1	AMDRY 9624 (Ni-based)	METCO 206A	323–340 cycles/ Delamination	350–678 cycles/ Delamination
B-2		METCO 206A /METCO 204C-NS	400–440 cycles/ Delamination	1127–1130 cycles/ Delamination
C-2		METCO 206A /METCO C-XCL	400–443 cycles/ Delamination	2000 cycles/ Sound condition

Table 3. EDS analysis for TGO layers developed after FCTF tests (at.%)

Sample & position	Ni	Co	Cr	Al	O	Total
B-1 (position 1)	1.03	1.90	1.72	37.72	57.63	100%
B-1 (position 2)	12.09	8.55	3.09	18.02	58.25	100%
B-2 (position 1)	2.23	-	4.13	35.26	58.38	100%
B-2 (position 2)	14.52	-	11.27	14.78	59.43	100%

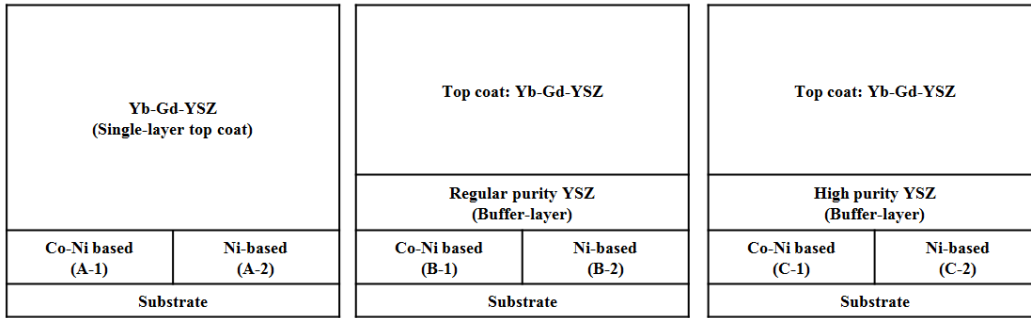


Fig. 1.

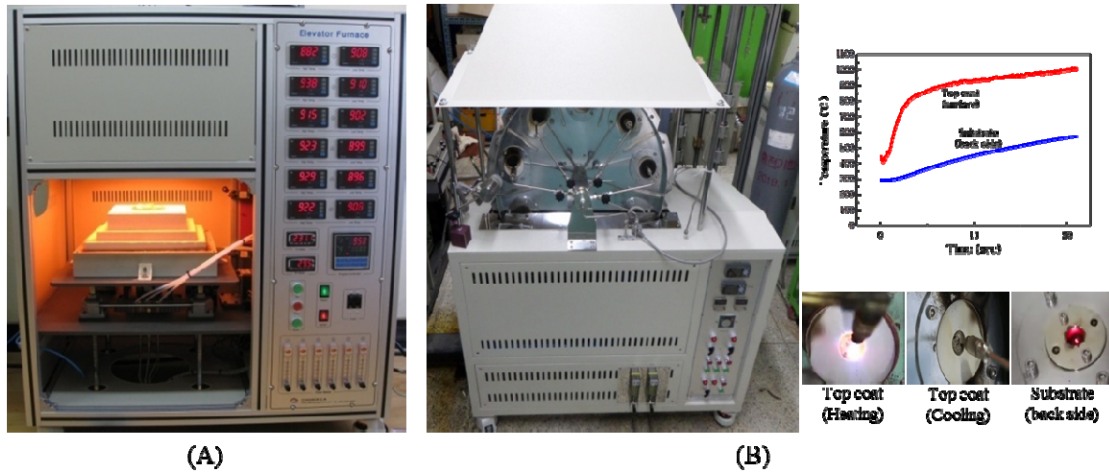


Fig. 2.

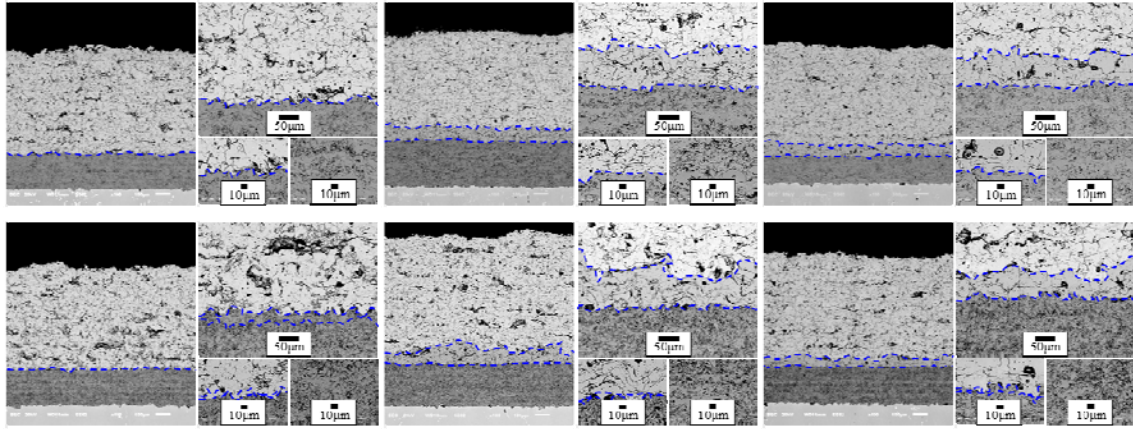


Fig. 3.

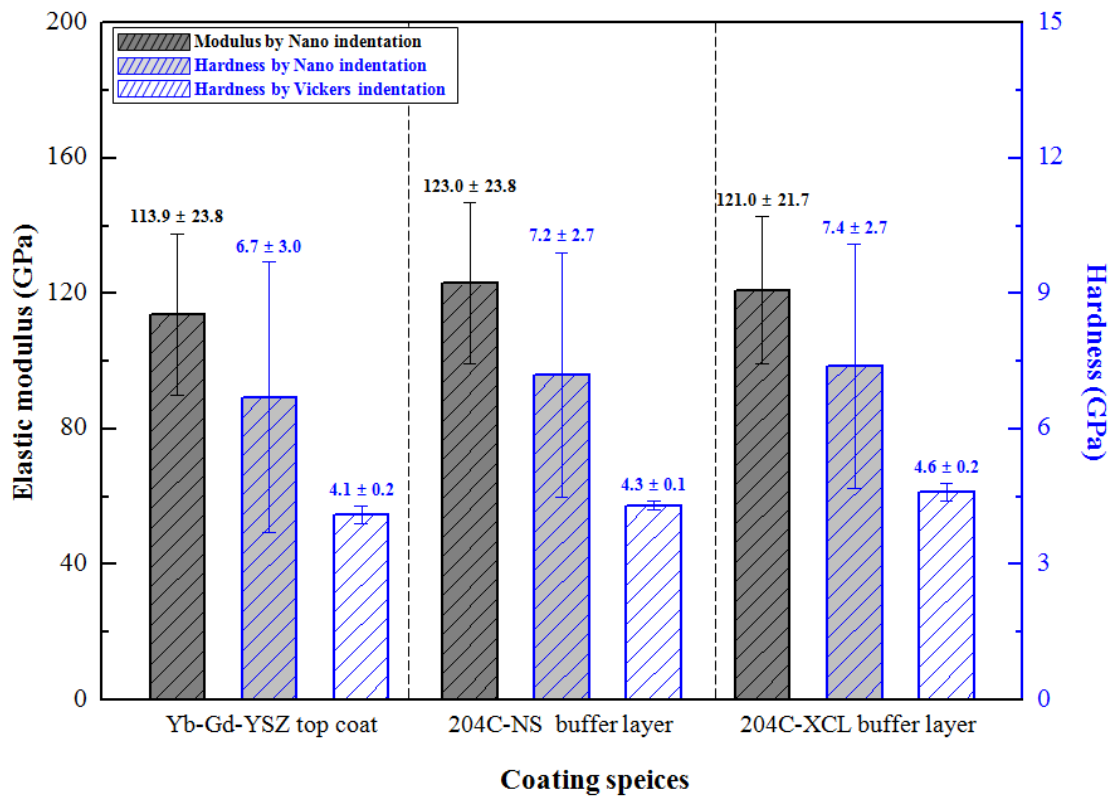


Fig. 4.

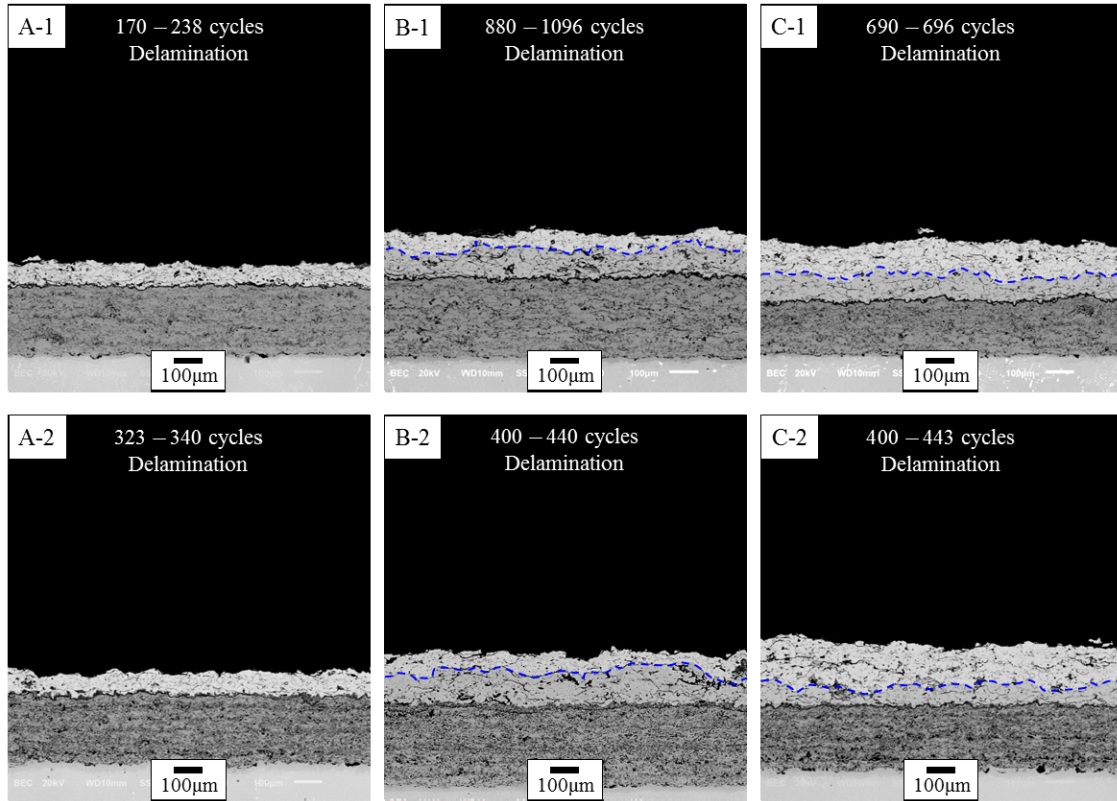


Fig. 5.

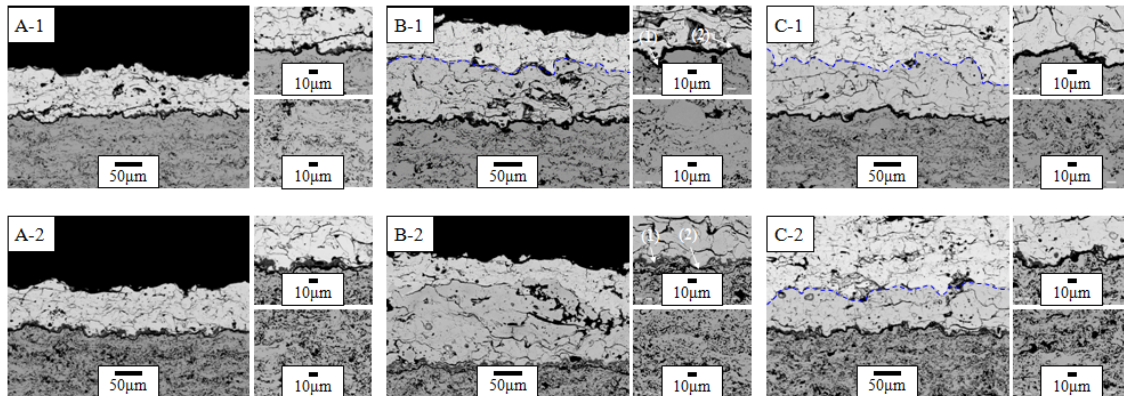


Fig. 6.

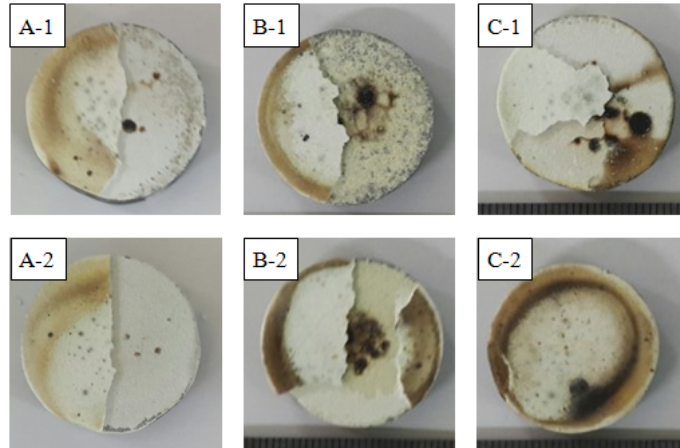


Fig. 7.

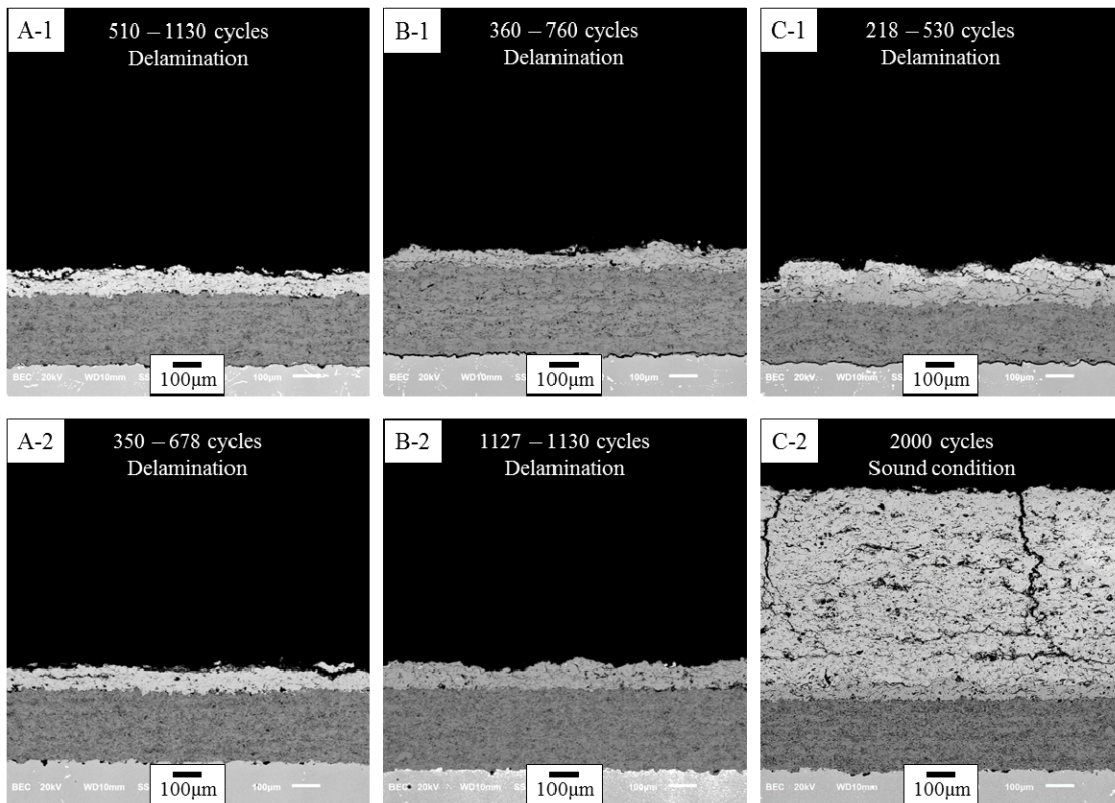


Fig. 8.

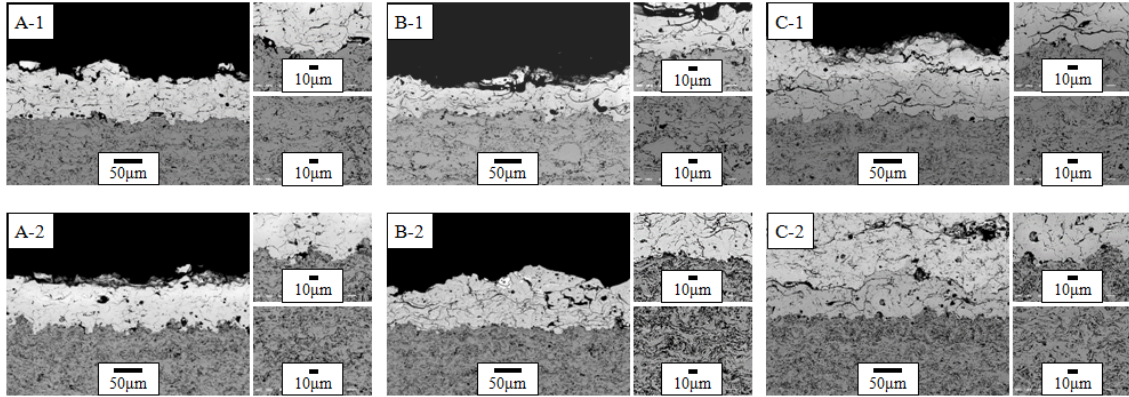


Fig. 9.

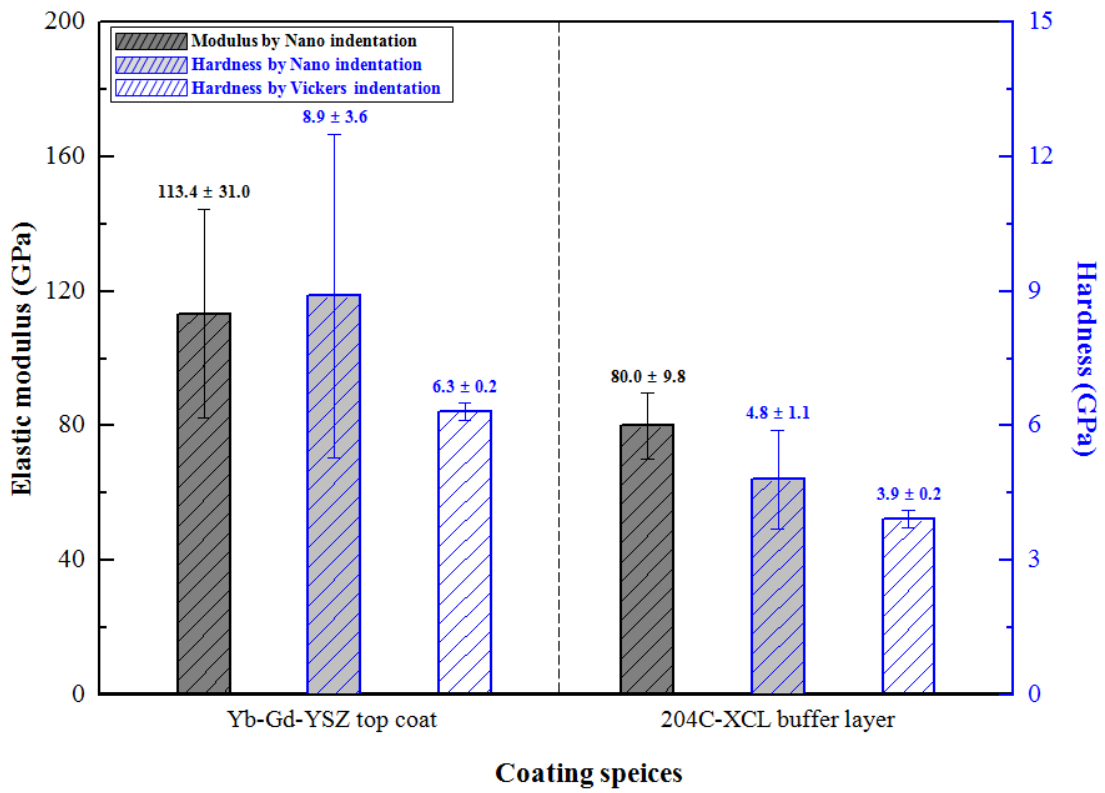


Fig. 10.